Supplementary Material for

Insight of Co and N statuses in the MOFs-derived porous carbonaceous materials on the catalytic ozonolysis at room temperature

Kun Wang[1], Binglin Xin[1], Runduo Zhang[*], Zhaoying Di, Bin Kang, Xiaonan Guo, Ying Wei, Jingbo Jia, Zhou-jun Wang

State Key Laboratory of Chemical Resource Engineering, Beijing Key Laboratory of Energy Environmental Catalysis, Beijing University of Chemical Technology, Beijing 100029, China

[*] Corresponding Author: zhangrd@mail.buct.edu.cn (Runduo Zhang)

[1] Kun Wang and Binglin Xin contribute equally as the first author for this work.

Content

S1. Figures

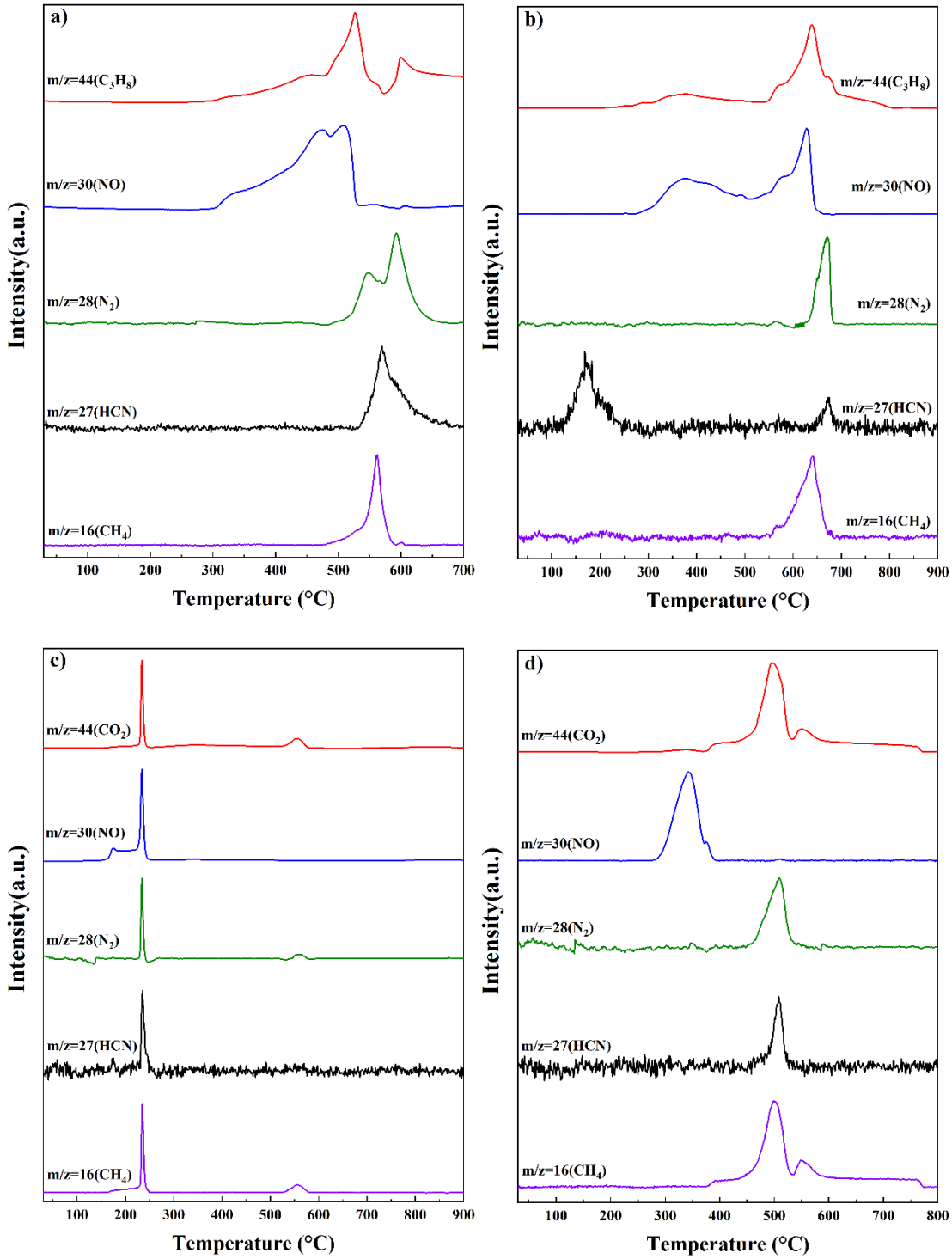
a)
m/z=44(C3H8)
m/z=30(NO)
m/z=28(N2)
m/z=27(HCN)
m/z=16(CH4)
Intensity(a.u.)
100 200 300 400 500 600 700
Temperature (°C)
b)
m/z=44(C3H8)
m/z=30(NO)
m/z=28(N2)
m/z=27(HCN)
m/z=16(CH4)
Intensity(a.u.)
100 200 300 400 500 600 700 800 900
Temperature (°C)
c)
m/z=44(CO2)
m/z=30(NO)
m/z=28(N2)
m/z=27(HCN)
m/z=16(CH4)
Intensity(a.u.)
100 200 300 400 500 600 700 800 900
Temperature (°C)
d)
m/z=44(CO2)
m/z=30(NO)
m/z=28(N2)
m/z=27(HCN)
m/z=16(CH4)
Intensity(a.u.)
100 200 300 400 500 600 700 800
Temperature (°C)

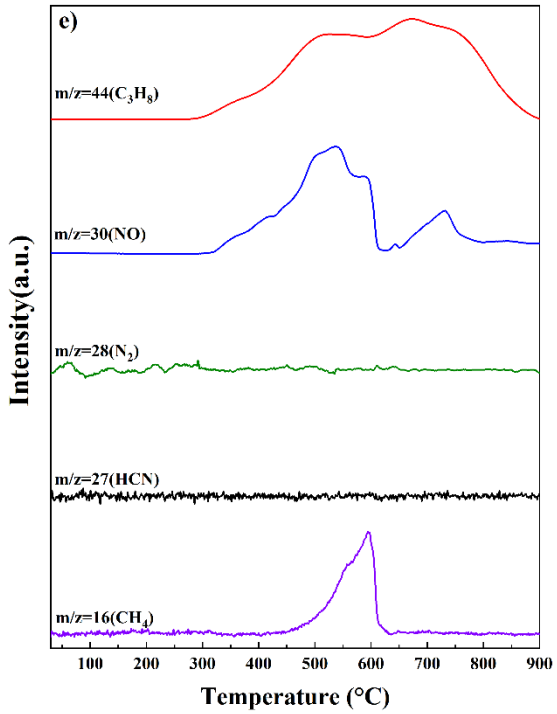

Figure. S1. Mass Spectrometry images of TGA a) ZIF-67, b) ZIF-9, c) ZIF-8-NC-$CO(NO_3)_2$, d) Co-BDC and e) ZIF-8

Figure S1 illustrated the species analysis of the tail gases from the TGA of ZIF-67, Co-BDC, ZIF-8, ZIF-9 and ZIF-8-NC-$CO(NO_3)_2$. The curves with core-to-mass ratios of 16, 27, 28, 30 and 44 corresponded to CH_4, HCN, N_2, NO and CO_2 or C_3H_8 species, respectively. NO and CH_4 were found in all samples. HCN and N_2 were found in ZIF-67, Co-BDC, ZIF-9 and ZIF-8-NC-$CO(NO_3)_2$, whereas were not found in ZIF-8. This may be due to the fact that the Zn-N structure in ZIF-8 is more stable and difficult to break. C_3H_8 with a nucleoplasm a ratio of 44 was found in ZIF-67, ZIF-8 and ZIF-9. CO_2 with a core-to-mass ratio of 44 was found in Co-BDC and ZIF-8-NC-$Co(NO_3)_2$. This difference was hypothesized to be related to the oxygen content of the samples. Large amounts of oxygen were present within Co-BDC and ZIF-8-NC-$Co(NO_3)_2$. While ZIF-67, ZIF-8 and ZIF-9 contained less oxygen. The C_3H_8 substance was produced under anaerobic conditions.

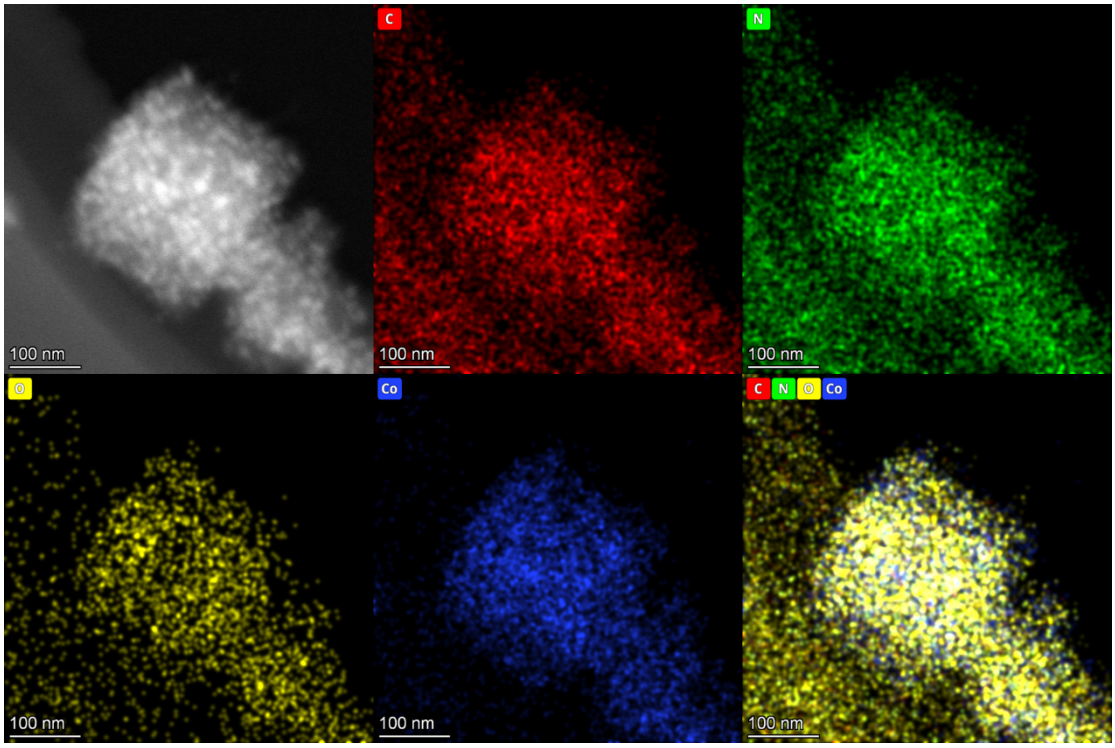

Figure. S2. Elemental mappings of ZIF-67-NC

The elemental mappings of ZIF-67-NC demonstrate the Co-existence and homogenous dispersion of C, N, O and Co elements.

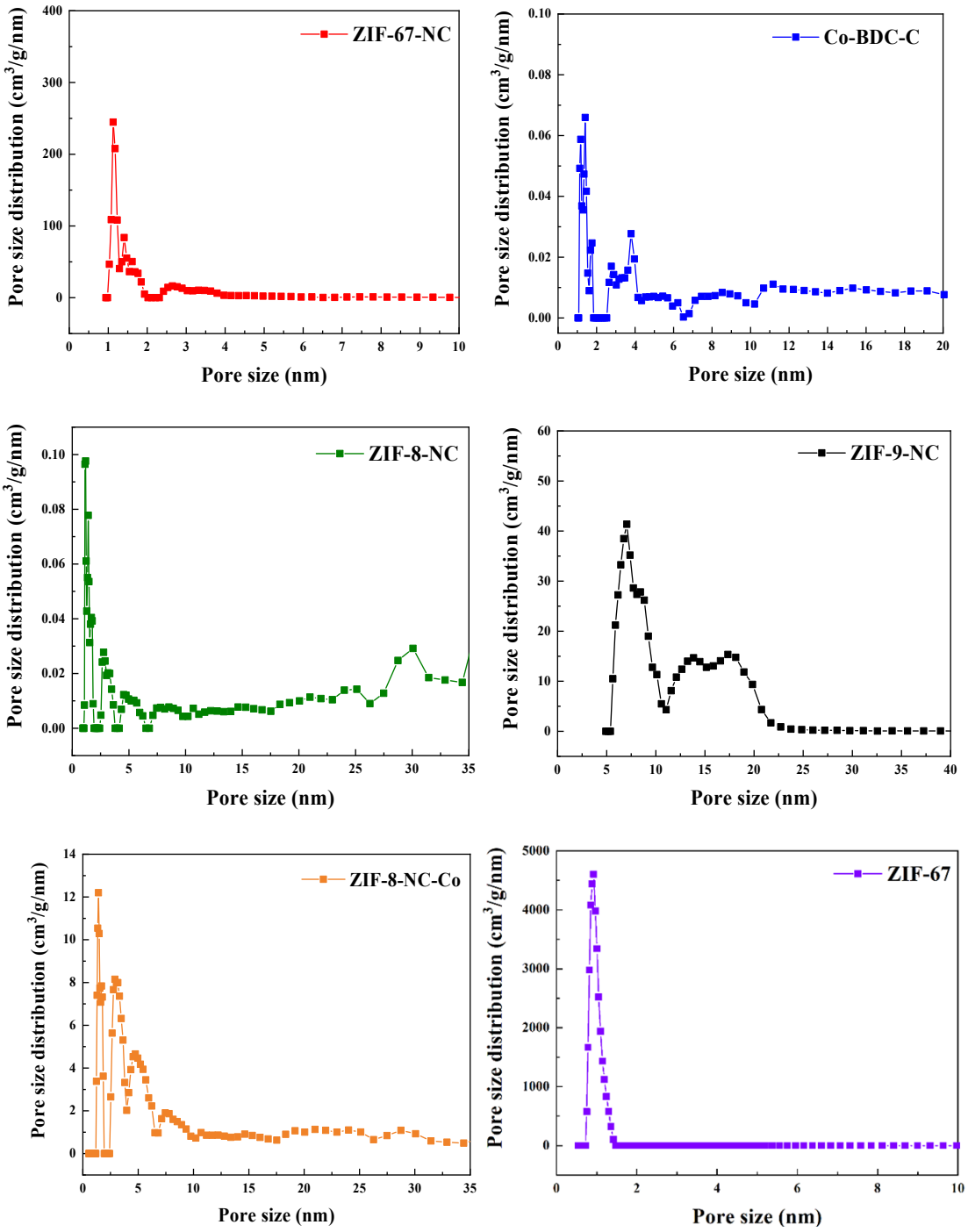

Figure S3. Pore size distribution of the prepared samples

The pore size distribution plots of the samples showed that the pores of ZIF-67 and ZIF-67-NC are mainly dominated by micropores, with a small amount of mesoporous structures. ZIF-9-NC and ZIF-8-NC-Co had a larger number of mesoporous structures and larger pores. ZIF-8-NC had a large number of mesoporous and microporous structures, which provides it with the largest specific surface area. The microporous and mesoporous structures were similar in proportion.

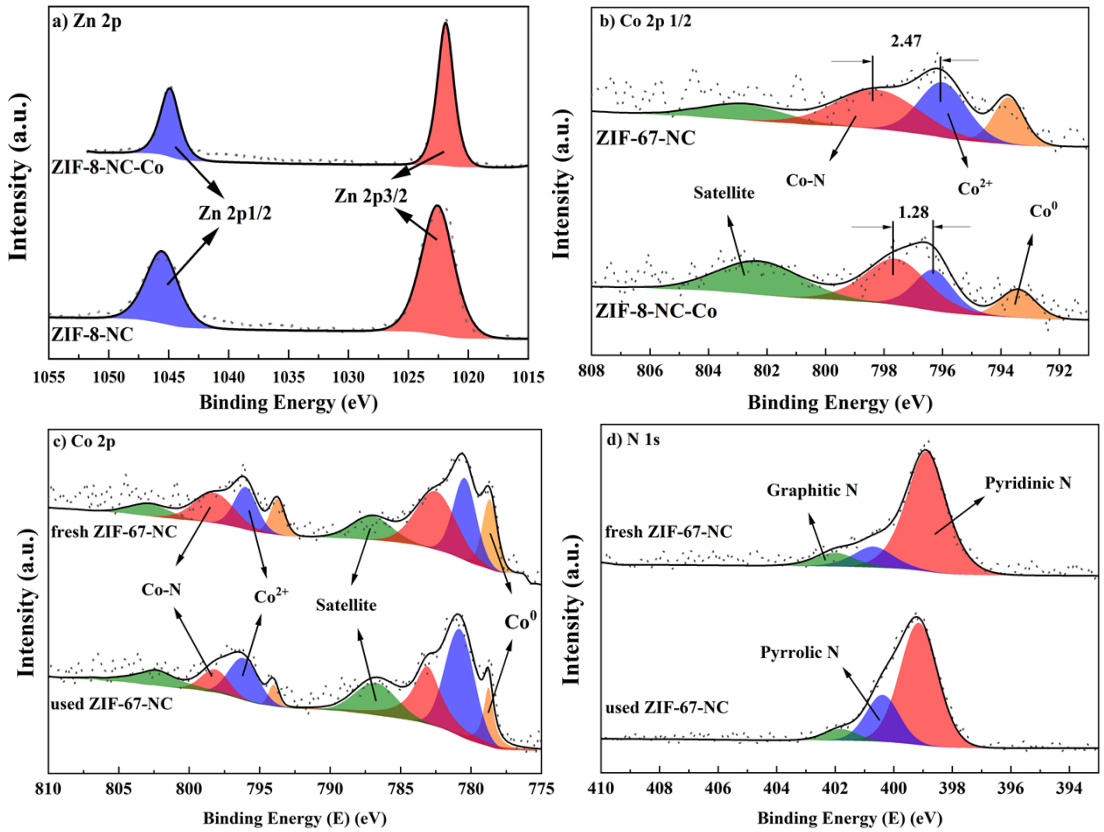

Figure S4. XPS of samples a) Zn 2p, b) Co 2p, c) Co 2p 1/2 of fresh and used ZIF-67-NC and d) N 1s of fresh and used ZIF-67-NC

The Zn 2p spectra have two Zn^{2+} 2p 1/2 (1044.8 eV) and Zn^{2+} 2p 3/2 (1021.8 eV). The shift of the Zn-2p spectrum of ZIF-8-NC-Co to a lower binding energy compared to ZIF-8-NC may be due to the difference in the coordination of Zn in Zn-N_4 and Co_3ZnC. The higher coordination number leads to the migration of the binding energy of Zn^{2+} to a lower binding energy. [S1, S6]

According to the literature, Luo pointed out that the Co-N peaks of XPS patterns are red-shifted with respect to the Co^{2+} ones, which represents a stronger electron exchange capacity and interaction of the Co-N bond than Co^{2+}-O bond [S6]. Presently, the red-shift of 2.47 eV of the Co2p 1/2 Co-N peaks with respect to the Co^{2+} peaks of ZIF-67-NC is indeed observed (see Figure S4b). Moreover, such a red-shift (2.47 eV) occurring over ZIF-67-NC is much higher than that occurring over ZIF-8-NC-Co (1.28 eV), suggesting the stronger electron exchange capacity for the former which is favorable for catalyzing the ozonolysis reaction.

Figure S4c and d show the XPS spectra of Co 2p and N 1s for fresh and used ZIF-

67-NC. The elemental content analysis of the two catalysts is shown in **Table S10**. The contents of Co-N and Co^0 in the used ZIF-67-NC slightly decrease, while the content of Co^{2+} increases. Meanwhile, the overall N content decreases. These data indicate that a small portion of Co-N and Co^0 is safely oxidized to Co^{2+} by ozone.

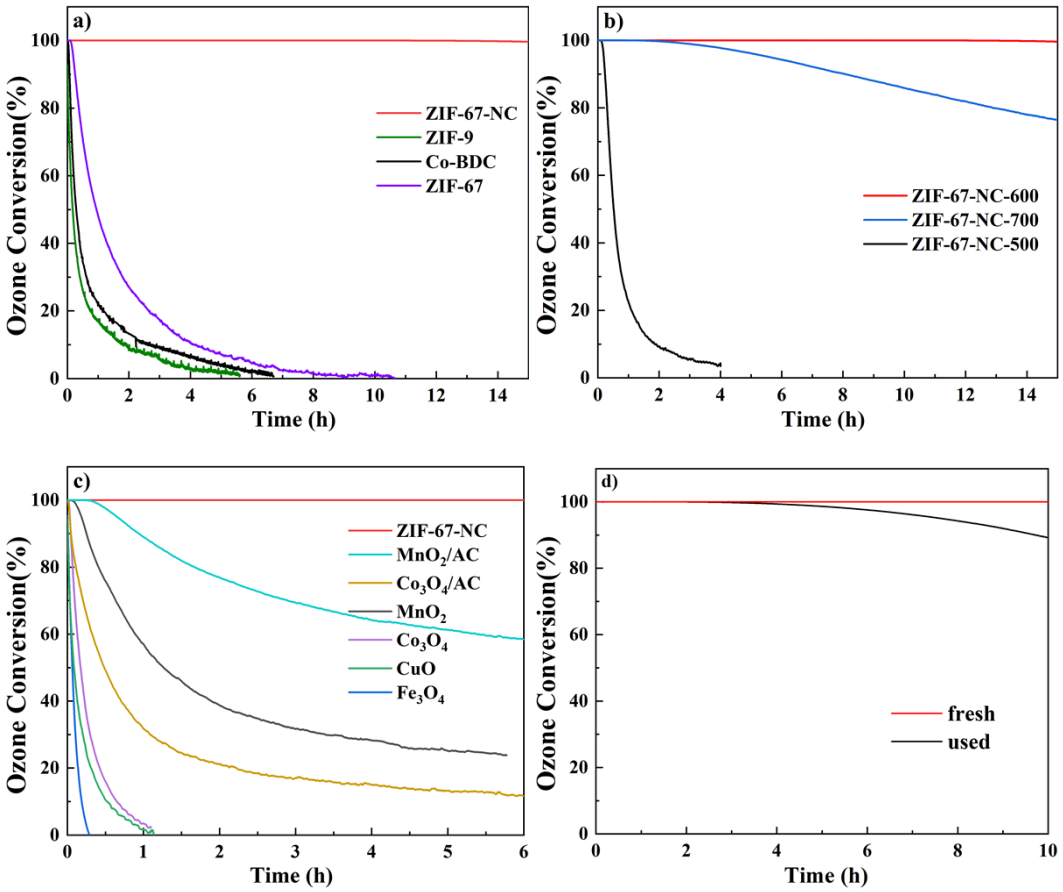

Figure S5. Catalytic performance of the catalysts for ozone decomposition. Reaction conditions: RH=50%, 40 ± 2 ppm O_3, WHSV=300 $L \cdot g^{-1} \cdot h^{-1}$, 25°C, a) ZIF-67-NC and MOFs, b) ZIF-67-NC obtained from different calcination temperatures, c) Traditional metal oxide catalysts and carbon-based catalysts, d) fresh and used of ZIF-67-NC catalysts.

Different cobalt-based MOFs were tested for catalytic ozonolysis activity. The results showed that all MOFs exhibited very poor catalytic ozonolysis activity. During the first two hours of catalytic decomposition, the catalytic activity of MOFs showed a sharp decrease. The ZIF-67 material was completely inactive after 10 hours of the reaction. The Co-BDC and ZIF-9 materials, on the other hand, showed a complete loss of catalytic activity after 6 hours. Organic ligands in MOFs were oxidized by adsorbed O_3 molecules. Therefore, the decrease in the catalytic ozone decomposition efficiency

of MOFs was due to the depletion of organic matter on the MOF surface. This is also related to the specific surface area of the parent material of the MOFs. A larger specific surface area resulted in a higher binding capacity of the catalyst to ozone. The superior specific surface area of ZIF-67 enhanced its ability to adsorb ozone molecules. Co-BDC and ZIF-9 had a smaller specific surface area and lower ozone adsorption capacity.

The three carbonized materials ZIF-67-NC-500, ZIF-67-NC-600, and ZIF-67-NC-700 obtained by pyrolysis of ZIF-67 at different temperatures are shown in Figure S5b. The activities of these three catalysts after 15 h under the experimental conditions (RH=50%, 40±2 ppm O_3, WHSV=300 $L \cdot g^{-1} \cdot h^{-1}$, 25 °C) were ZIF-67-NC-600 (100%) > ZIF-67-NC-700 (78.5%) > ZIF-67-NC-500 (0%). Therefore, 600 °C was selected as the optimal pyrolysis temperature for ZIF-67 based on the corresponding superior performance for ZIF-67-NC-600 (100%). Based on the analysis of the pyrolysis curves and products of ZIF-67 in Figure 3 and Table 1, the following conclusions can be drawn: when the pyrolysis temperature was lower than 600 °C, the decomposition of ZIF-67 ligand was mainly accomplished. The Co atoms was seriously encapsulated by organic ligands of ZIF precursor, which led to an essentially poor activity of ZIF-67-NC-500 (0%). When the pyrolysis temperature reaching 700 °C, the successive N releasing from ZIF-67 severely damaged the Co-N structure and reduced the total number of active sites in the catalyst, as indicated by the secondary peak of line m/z=28 (N_2) of Figure S1.

Figure S5c demonstrates the ozonolysis activity of ZIF-67-NC, conventional metal oxides and carbon-based catalysts. From the figure, it can be seen that the catalytic activities of activated-carbon-supporting oxides (Co_3O_4/AC and MnO_2/AC) have been improved as compared with those of simple metal oxides (Co_3O_4, MnO_2). ZIF-67-NC obtained from the pyrolysis of ZIF-67 has excellent catalytic activity, which is a significant advantage over the other catalysts.

As shown in Figure S5d, the catalytic activity of the used ZIF-67-NC decreased to 89.8% after 10 h continuous catalytic activity test. The used ZIF-67-NC had great stability and catalytic activity.

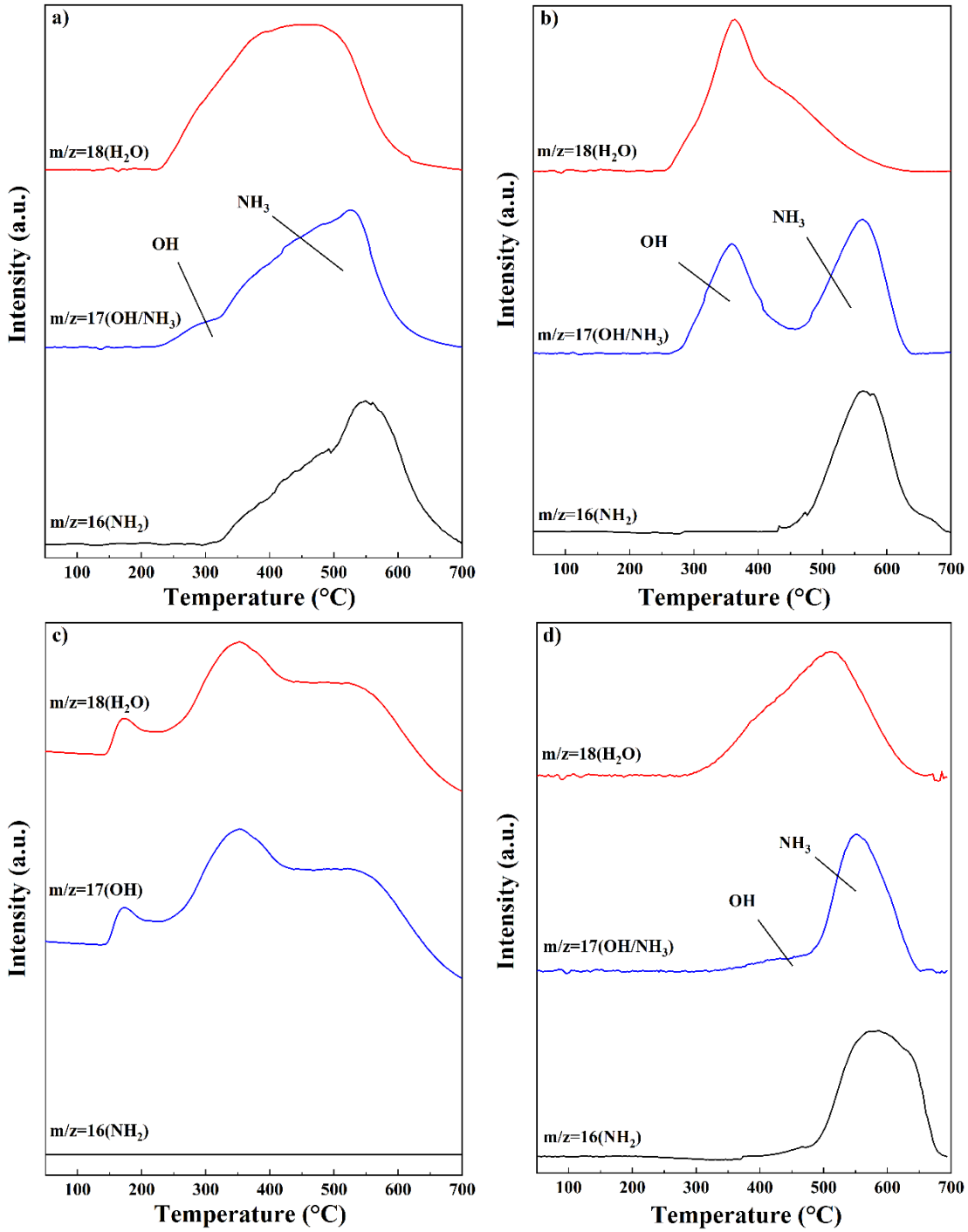

Figure S6. Mass Spectrometry images of H_2-TPR: ZIF-67-NC (a), ZIF-8-NC-Co (b), Co-BDC-C (c) and ZIF-9-NC (d)

As shown in **Figure S6**, the peak in the m/z = 16 (NH_2) curve indicates the reduction of the Co-N structure. The peak in the m/z = 18 (H_2O) curve indicates the reduction of the Co^{2+}-O structure. The higher reduction temperature of the Co-N structure indicates that it has a higher bond energy and is more difficult to be reduced compared to the Co^{2+}-O structure.

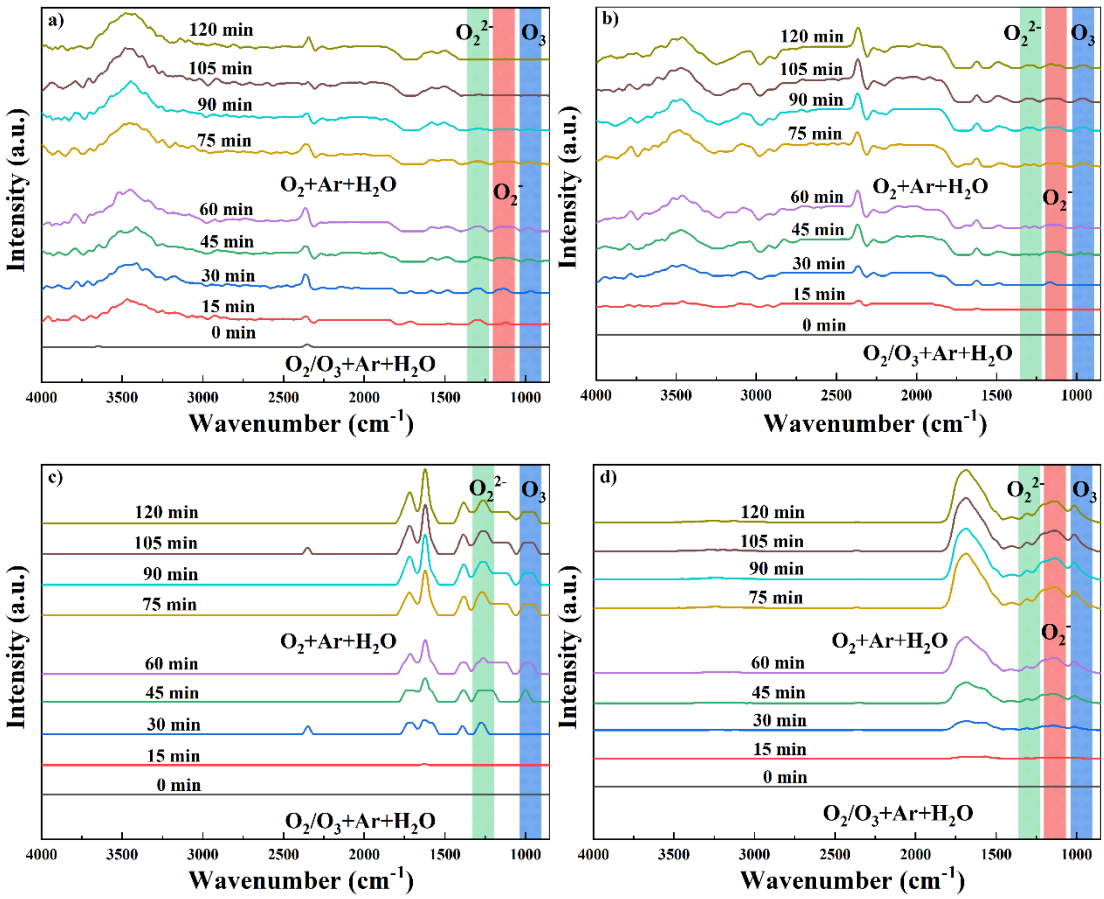

Figure. S7. In situ DRIFTs spectra of ZIF-67-NC (a), ZIF-8-NC-Co (b), Co-BDC-C (c) and ZIF-9-NC (d) in RH=50% conditions

Figure S7 exhibited the O_3-DRIFTs spectra of ZIF-67-NC, ZIF-8-NC-Co, Co-BDC-C and ZIF-9-NC. The peaks near 3000-3700 cm^{-1} and 1500-1700 cm^{-1} were associated with the stretching vibration of hydroxyl group and the bending vibration of H_2O related. [S2, S3] The peaks in this part of the spectrum are mainly due to the adsorption of KBr on water in the pipeline, which produces the peaks of hydroxyl and H_2O. The peaks at 1200-1400 cm^{-1} were related to the production of O_2^{2-} during O_3 decomposition. [S3, S4] The peaks from 900-1100 cm^{-1} were related to the adsorption of O_3 on the catalysts surface. [S5, S6]

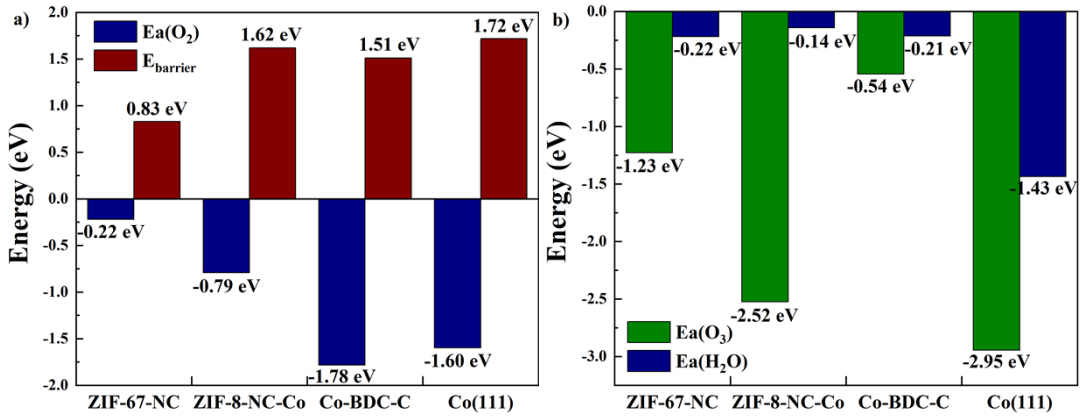

Figure. S8. a) $Ea(O_2)$ and $E_{barrier}$, b) $Ea(O_3)$ and $Ea(H_2O)$ of ZIF-67-NC, ZIF-8-NC-Co, Co-BDC-C and Co(111)

A graphene sheet model was used to simulate the carbon carriers. Four carbon-loaded Co-N_x (x = 1, 2, 3, and 4) were modeled with cell sizes a = 12.300 Å, b = 9.840 Å, and c = 20.000 Å. The K-points in the Brillioun zone were selected by the Monkhorst-Pack method, and the Co-N_x was set to be 3 × 3 × 1Γ.

The Co^0 (111) supercell model was obtained by extending a single Co0 cell after cutting it along the (111) crystal plane. Cell dimensions were a = 9.558 Å, b = 9.558 Å, and c = 19.342 Å to prevent interactions with periodically repeating images. During geometry optimization, atoms in the top two layers were allowed to relax while atoms in the remaining layers remained fixed in the optimized positions. K-points in the Brillioun zone were selected by the Monkhorst-Pack method with Co^0 (111) set to 18 × 18 × 8 Γ.

The Co_3ZnC supercell model was obtained by extending a single Co_3ZnC cell after cutting it along the (111) crystal plane. The cell dimensions were a = 10.833 Å, b = 10.833 Å and c = 21.634 Å to prevent interactions with periodically repeating images. During geometry optimization, atoms in the top two layers were allowed to relax while atoms in the remaining layers remained fixed in the optimized positions. K-points in the Brillioun zone were selected by the Monkhorst-Pack method with Co_3ZnC set to 4 × 4 × 1Γ.

The Co_3O_4 supercell model was obtained by extending a single Co_3O_4 cell after cutting it along the (111) crystal plane. The cell dimensions were a = 11.376 Å, b = 11.376 Å and c = 15.000 Å to prevent interactions with periodically repeating images.

During geometry optimization, atoms in the top two layers were allowed to relax while atoms in the remaining layers remained fixed in the optimized positions. K- points in the Brillioun zone were selected by the Monkhorst-Pack method with Co_3O_4 set to 3 × 3 × 2 Γ.

In addition, free O_3 and O_2 molecules were modeled in a periodic box of 10 × 10 × 10 Å3 to ensure that interactions with their images in adjacent cells were negligible. 3 × 3 × 1 Γ central k-points have been used for O_3 molecular geometry optimization. 3 × 1 × 1 Γ central k-points have been used for O_2 molecular geometry optimization.

To accurately acquire the images of transition states (TS), the climbing-image nudged elastic band (CI-NEB) method was first employed to search for transition states with a loose convergence criterion (0.5 eV/Å) for fast convergence. Next, the images found in the first step are refined using the Improved Dimer Method (IDM) until the force converges to 0.05 eV/Å to obtain more accurate transition state structures.

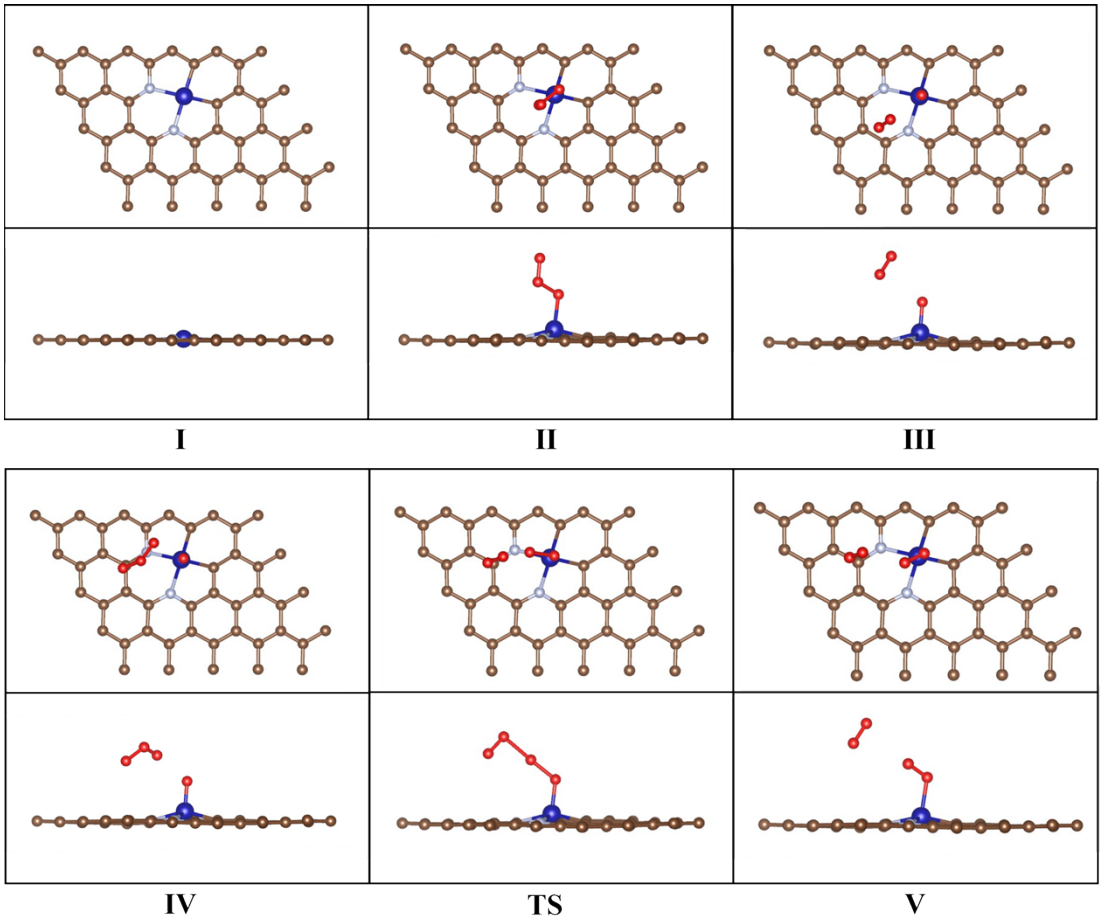

Figure. S9. The reaction pathway for the O_3 molecule decomposition on the ZIF-67-NC.

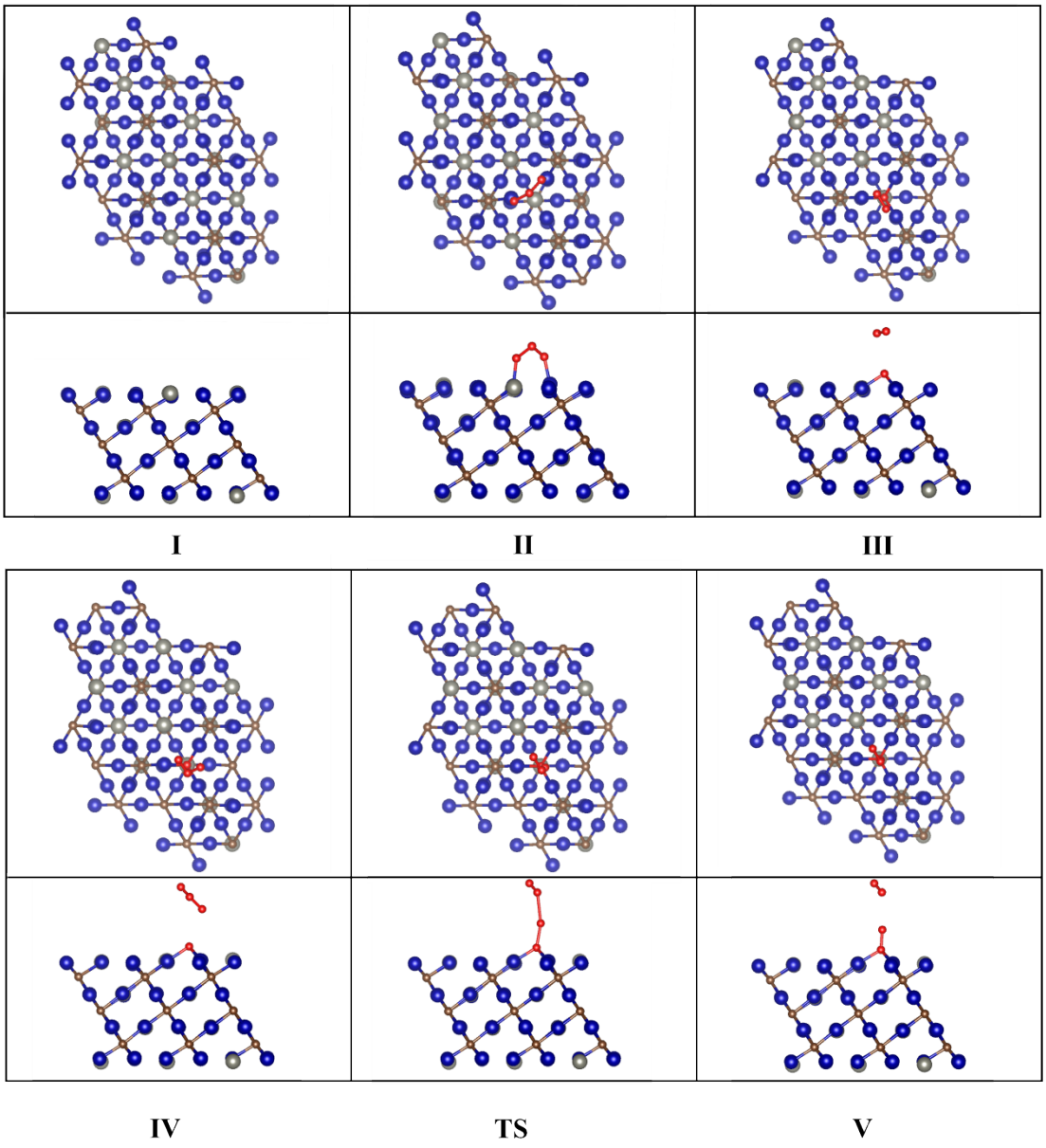

Figure. S10. The reaction pathway for the O_3 molecule decomposition on the ZIF-8-NC-Co.

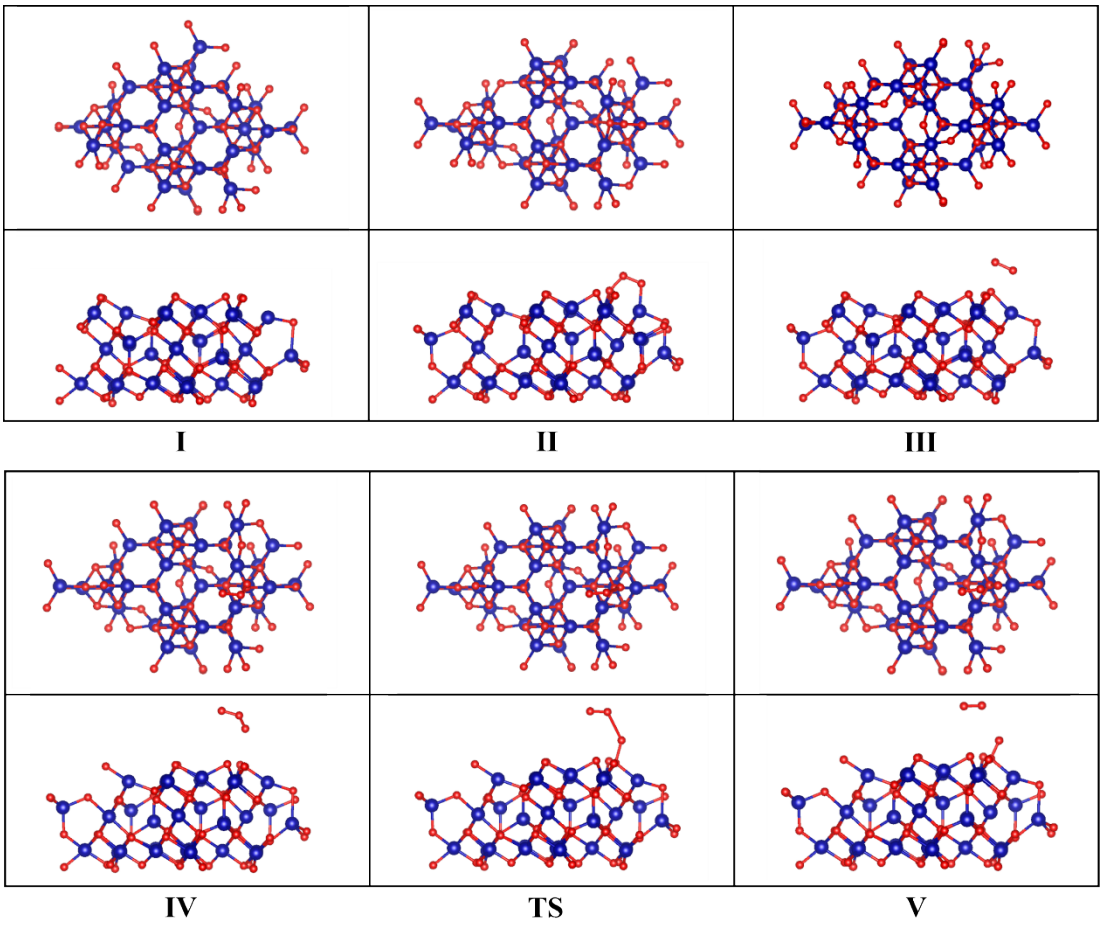

Figure. S11. The reaction pathway for the O_3 molecule decomposition on the Co-BDC-C.

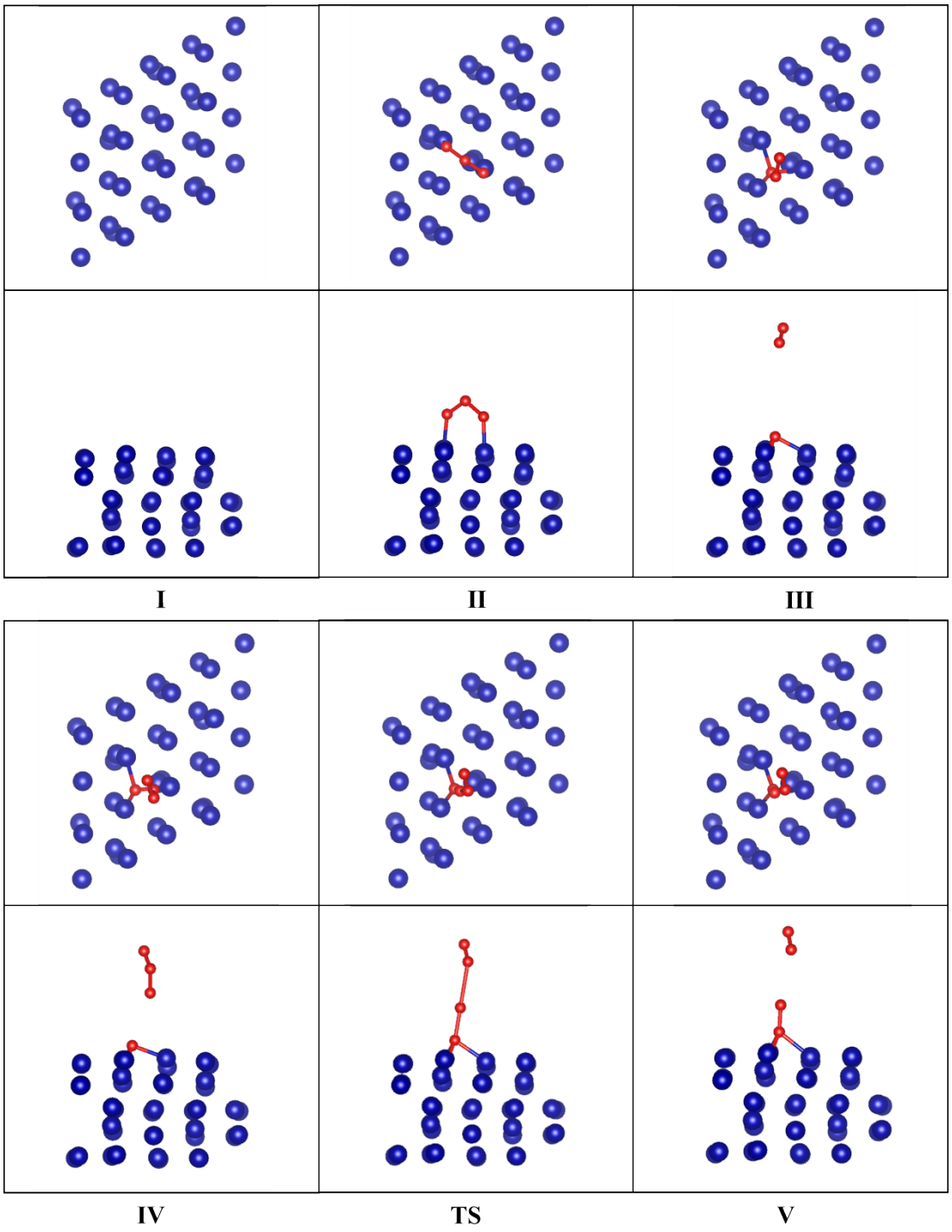

Figure. S12. The reaction pathway for the O_3 molecule decomposition on the Co.

S2. Tables

Table. S1. C Elemental content of samples determined by XPS

(%)	C=C	C-O/N	C=O	π-π*
ZIF-67-NC	56.69	29.72	8.55	5.04
Co-BDC-C	84.84	6.96	4.43	3.76
ZIF-9-NC	75.55	16.77	4.61	3.07
ZIF-8-NC	59.28	29.00	9.65	2.07
ZIF-8-NC-Co	68.86	17.99	7.03	6.11
ZIF-67	77.98	17.61		4.41

Table. S2. N Elemental content of samples determined by XPS

(at%)	N 1s	Pyridinic-N	Pyrrolic-N	Graphitic-N	N-O
ZIF-67-NC	14.36	11.13	1.95	1.28	0.28
Co-BDC-C	1.22				
ZIF-9-NC	13.54	8.67	1.91	2.45	0.51
ZIF-8-NC	20.49	12.04	7.10	1.35	
ZIF-8-NC-Co	13.75	10.64	2.67	0.44	
ZIF-67	27.08	17.18	9.11	0.80	

Table. S3. O Elemental content of samples determined by XPS

(at%)	O 1s	Metal Oxides	Absorbed Oxygen	Absorbed Water/Hydroxyl
ZIF-67-NC	10.97	0.79	7.00	3.18
Co-BDC-NC	9.39	2.44	5.21	1.74
ZIF-9-NC	5.59	0.38	3.79	1.41
ZIF-8-NC	9.87	0.29	6.05	3.53
ZIF-8-NC-Co	17.45	0.99	15.02	1.44
ZIF-67	3.37		3.03	0.34

Table. S4. Specific surface area and elemental analysis of the catalysts

Catalyst	S_{BET} [a] (m^2/g)	S_{mic} [b] (m^2/g)	S_{ext} [b] (m^2/g)	S_{mes} [c] (m2/g)	Average pore size [d] (nm)	V_{total} [d] (cm^3/g)	V_{mic} [b] (cm^3/g)	V_{mes} [e] (cm^3/g)
ZIF-67-NC	401	311	90	45	3.65	0.366	0.127	0.209
ZIF-8-NC-Co	75	0	75	75	20.1	0.382	0	0.372
Co-BDC-C	284	199	85	71	5.06	0.359	0.083	0.265
ZIF-9-NC	539	39	500	160	3.01	0.408	0.018	0.183
ZIF-8-NC	597	463	134	110	8.12	1.270	0.187	1.066
ZIF-67	1902	1833	69	35	1.82	0.870	0.674	0.174

[a] Brunauer-Emmett-Teller (BET) surface area.

[b] *t*-plot (p/p_0 from 0.2 to 0.5).

[c] BJH (p/p0 from 0.35 to 0.995)

[d] The volume absorbed at $p/p_0 = 0.99$.

[e] Barrett-Joyner-Halenda (BJH) is calculated by desorption data.

The relationship of specific surface area calculated according to the Brunauer-Emmett-Teller (BET) method is: ZIF-8-NC (597 m^2/g) > ZIF-9-NC (539 m^2/g) > ZIF-67-NC (401 m^2/g) > Co-BDC-C (284 m^2/g) > ZIF-8-NC-Co (75 m^2/g). This may be related to differences in the nitrogen and oxygen content of the organic ligands. High nitrogen content organic ligands are not easily destroyed during carbonization and can maintain part of the pore structure. The high oxygen content organic ligand is more eroded by oxygen during carbonization, and the pore structure is more likely to collapse. This resulted in a larger specific surface area after carbonization of MOFs with high nitrogen content.

Table S5. Elemental contents of the as-prepared catalysts determined by Elemental analysis and ICP

Catalyst	C [a] (at%)	N [a] (at%)	O [a] (at%)	Co [b] (at%)	Zn [b] (at%)
ZIF-67-NC	39.78	11.49	12.64	36.08	
ZIF-8-NC-Co	22.54	8.73	17.54	28.14	23.05
Co-BDC-C	37.37	0	11.33	51.29	
ZIF-9-NC	51.47	16.80	5.66	26.07	
ZIF-8-NC	37.00	22.59	11.09		29.32
ZIF-67	42.21	24.97	3.29	29.54	

[a] Measured by Elemental analysis.

[b] Measured by ICP-AES.

Table S6. H_2 consumption of the samples

Catalyst	Temperature / °C & H_2 consumption / μmol/g							
	Peak α [a] CoO to Co		Peak β Co^{2+} to Co		Peak γ CH_4/NH_3		Peak λ Co^{3+} to Co^{2+}	
ZIF-67-NC	321	892	440	1560	575	642		
ZIF-8-NC-Co	308	727	463	924	530	314		
Co-BDC-NC	360	662	518	1729	624	264	225	581
ZIF-9-NC	425	548	528	616	610	229	□	□

[a] The H_2 consumption of Peak α represents the amount of CoO.

Table S7. H_2 consumption of the samples

Catalyst	isolated /μmol/g [a] CoO	isolated /μmol/g [b] Co^{2+}	isolated /μmol/g [c] Co^{3+}	Total H_2 consumption /μmol/g [d]
ZIF-67-NC	892	1560.0		3094.3
ZIF-8-NC-Co	727	923.7		1964.8
Co-BDC-NC	662	568.0	1741.6	3235.5
ZIF-9-NC	548	616.0		1393.0

[a] Isolated CoO = H_2 consumption of Peak α.

[b] Isolated Co^{2+} = H_2 consumption of (Peak β − 2 × Peak λ).

[c] Isolated Co^{3+} = 3 × H_2 consumption of Peak λ.

[d] Total H_2 consumption = H_2 consumption of (Peak α + Peak β + Peak γ + Peak λ).

Table S8. H_2O desorption percentage of the samples

Catalyst	Temperature / °C & H_2O Desorption Capacity (μg/g)						
	Peak α	Peak β_1	Peak β_2	**Peak γ**	Peak λ_1	Peak λ_2	Peak λ_3
ZIF-67-NC	12.19 (81°C)	8.7 (116°C)	2.8 (171°C)	**2.2 (227°C)**	4.4 (289°C)	1.6 (380°C)	
ZIF-8-NC-Co	1.6 (75°C)	19.8 (125°C)	5.5 (181°C)	**6.0 (233°C)**	6.6 (308°C)		
Co-BDC-C		4.0 (148°C)	9.4 (175°C)	**6.4 (240°C)**	3.8 (302°C)	1.5 (372°C)	1.1 (439°C)

Table S9. Adsorption energy of O_3, H_2O and O_2 and $E_{barrier}$

	$E_a(O_3)$(eV)	**$E_a(H_2O)$ (eV)**	**$E_a(O_2)$ (eV)**	**$E_{barrier}$(eV)**
Co-N_1	-0.8315	-0.1967	-0.2273	0.89
Co-N_2	-1.2287	-0.2185	-0.2205	0.83
Co-N_3	-1.2804	-0.2075	0.0381	0.96
Co-N_4	-1.5675	-0.2838	0.2124	0.91

Table S10. Elemental content of Catalysts determined by XPS

Catalyst	C 1s	N 1s	O 1s	Co 2p	Co^0	Co^{2+}	Co-N
	(at%)	(at%)	(at%)	(at%)	(at%)	(at%)	(at%)
fresh ZIF-67-NC	69.24	14.36	10.97	5.43	1.07	1.94	2.42
used ZIF-67-NC	67.93	12.01	15.42	4.64	0.44	2.33	1.87

References

S1. L. Wu, X. Wang, P. Zhao, Y. Ji, B. Li, Y. Xu, et al., Nanoconfinement-induced high activity of ZIF-8 derived atomic Zn-N-C materials for fenton-like reactions. *Chem. Eng. J.* **2024,** *489,* 151395.

S2. Z. Xu, W. Yang, W. Si, J. Chen, Y. Peng, J. Li, A novel gamma-like MnO_2 catalyst for ozone decomposition in high humidity conditions. *J. Hazard. Mater.* **2021,** *420*, 126641.

S3. H. Valdés, F. J. Ulloa, V. A. Solar, M. S. Cepeda, F. Azzolina-Jury, F. Thibault-Starzyk, New insight of the influence of acidic surface sites of zeolite on the ability to remove gaseous ozone using operando DRIFTS studies. *Microporous Mesoporous Mater.* **2020,** *294*, 109912.

S4. J. Wu, T. Su, Y. Jiang, X. Xie, Z. Qin, H. Ji, In situ DRIFTS study of O_3 adsorption on CaO, γ-Al_2O_3 , CuO, α-Fe_2O_3 and ZnO at room temperature for the catalytic ozonation of cinnamaldehyde. *Appl. Surf. Sci.* **2017,** *412*, 290-305.

S5. G. Berlier, T. Yamamoto, G. Spoto, C. Lamberti, E. Gribov, A. Zecchina, IR spectra of ozone adsorbed on MgO. *Phys. Chem. Chem. Phys.* **2002,** *4(15)*, 3872-3875.

S6. Y. Luo, S. Liu, M. Chen, Y. He, W. Zhang, et al., Bimetallic synergistic catalysis strategy with one-dimensional CuCo-NC for enhanced Wide-temperature stability in high-energy lithium-sulfur batteries. *Chem. Eng. J.* **2025**, *505*, 159158.